https://doi.org/10.5194/gmd-2023-35
Preprint. Discussion started: 4 April 2023
© Author(s) 2023. CC BY 4.0 License.

Geoscientific Model Development Discussions

Rapid assimilations of O_3 observations – Part 1: methodology and tropospheric O_3 changes in China in 2015-2020

Rui Zhu[1], Zhaojun Tang[1], Xiaokang Chen[1], Zhe Jiang[1]* and Xiong Liu[2]

[1]School of Earth and Space Sciences, University of Science and Technology of China, Hefei, Anhui, 230026, China.
[2]Center for Astrophysics | Harvard & Smithsonian, Cambridge, MA 02138, USA.

*Correspondence to: Zhe Jiang (zhejiang@ustc.edu.cn)

Abstract

The high computational cost of chemical transport models (CTMs) is a potential bottleneck for the rapid assimilation of ozone (O_3) observations. Here we developed a single tracer tagged-O_3 mode to build the capability of the GEOS-Chem model for rapid simulation of tropospheric O_3. The tagged-O_3 mode demonstrates high consistency with GEOS-Chem full-chemistry simulation and dramatic reductions in computational costs by approximately 91-94%. The tagged-O_3 simulation was combined with China Ministry of Ecology and Environment (MEE) and Ozone Monitoring Instrument (OMI) O_3 observations to investigate the changes in tropospheric O_3 over E. Asia in 2015-2020. The assimilated O_3 concentrations demonstrate good agreement with O_3 observations: surface O_3 concentrations are 42.9, 41.8 and 42.1 ppb; and tropospheric O_3 columns are 37.1, 37.9 and 38.0 DU in the simulations, assimilations and observations, respectively. The assimilations indicate rapid increases in surface O_3 by 1.60 (spring), 1.16 (summer), 1.47 (autumn) and 0.80 (winter) ppb yr^{-1} over E. China in 2015-2020, and the increasing trends are underestimated by the a priori simulations. More attention is thus suggested to the rapid increases in O_3 pollution in spring and autumn. Furthermore, we find stronger increases in tropospheric O_3 columns over highly polluted areas, which may reflect the larger contributions of local emissions. The large discrepancy in the trends in tropospheric O_3 columns by assimilating surface and satellite observations further indicates the possible uncertainties in the derived free tropospheric O_3 changes. The rapid O_3 assimilation capability

https://doi.org/10.5194/gmd-2023-35
Preprint. Discussion started: 4 April 2023
© Author(s) 2023. CC BY 4.0 License.

Geoscientific Model Development Discussions

is a useful tool for the extension and interpretation of atmospheric O_3 observations.

1. Introduction

Tropospheric ozone (O_3) is an important pollutant with significant adverse effects on human health and crop growth (Zhang et al., 2021; Li et al., 2022). Tropospheric O_3 is produced when volatile organic compounds (VOC) and carbon monoxide (CO) are photochemically oxidized in the presence of nitrogen oxides (NO_x). Chemical transport models (CTMs) are widely used to simulate tropospheric O_3 variabilities (Jiang et al., 2015; Zhang et al., 2016; Xue et al., 2021). Considering the uncertainties in physical and chemical processes (Peng et al., 2021; Chen et al., 2022) and emission inventories (Elguindi et al., 2020; Jiang et al., 2022), remotely sensed O_3 observations are further applied to improve the modeled O_3 concentrations via data assimilation techniques (Huijnen et al., 2020; Colombi et al., 2021). In addition to satellite observations, surface stations provide valuable information for air quality by producing high-accuracy in situ measurements. For example, Ma et al. (2019) found that the assimilation of surface observations can effectively improve the predicted surface O_3 concentrations; Peng et al. (2018) obtained good forecasts in short-term surface O_3 variabilities by assimilating surface observations.

The description of O_3 photochemistry in CTMs can provide useful constraints on O_3 concentrations in assimilations (van Peet et al., 2018; Miyazaki et al., 2020). However, the high computational cost is a potential bottleneck for rapid assimilations with high spatial resolution and wide spatial coverage, which poses a possible barrier to better understanding the long-term changes in tropospheric O_3 on continental or global scales. Alternatively, people may consider simulations of atmospheric O_3 with the archived O_3 product and loss rates. For example, the tagged-O_x mode of the GEOS-Chem model has been used to analyze the sources and transport of tropospheric O_3 (Zhang et al., 2008; Zhu et al., 2017; Han et al., 2018). However, it may not

https://doi.org/10.5194/gmd-2023-35
Preprint. Discussion started: 4 April 2023
© Author(s) 2023. CC BY 4.0 License.

Geoscientific Model Development Discussions

be an ideal choice to perform O_3 assimilations based on the tagged-O_x mode because O_x is the combination of multiple species, including O_3, and thus cannot be accurately compared with O_3 observations.

In this study, we developed the single tracer tagged-O_3 mode of the GEOS-Chem model, driven by archived O_3 product and loss rates provided by GEOS-Chem full chemistry simulations, to build the capability of the GEOS-Chem model for rapid simulations of tropospheric O_3 (rather than O_x). The tagged-O_3 simulation was then combined with the Ozone Monitoring Instrument (OMI) and China Ministry of Ecology and Environment (MEE) monitoring network O_3 observations (in this paper) and United States (US) Air Quality System (AQS) and European AirBase network O_3 observations (in the companion paper: Part 2, Zhu et al. (2023)) via a sequential Kalman Filter (KF) assimilation system (Tang et al., 2022; Han et al., 2022) to investigate the performance of single tracer simulation on O_3 assimilations. Furthermore, the rapid assimilation capability based on the tagged-O_3 mode allows us to perform a convenient, comparative analysis to investigate the changes in tropospheric O_3 in E. China in 2015-2020 (in this paper) and the US and Europe in 2005-2020 (in the companion paper: Part 2, Zhu et al. (2023)). Considering their different vertical sensitivities, a comparative analysis by assimilating satellite and surface O_3 measurements is useful for better characterization of O_3 changes in the surface and free troposphere and is helpful for better applications of satellite and surface O_3 measurements in the future.

This paper is organized as follows: in Section 2, we describe the surface (MEE, AQS and AirBase) and OMI O_3 observations, GEOS-Chem model and data assimilation system used in this work. Tropospheric O_3 changes in E. China in 2015-2020 are then demonstrated in Section 3 by assimilating MEE and OMI O_3 observations. As shown in Fig. 1, five regions (i.e., North China Plain (#1), Yangtze River Delta (#2), Central China (#3), Sichuan Basin (#4) and Southern China (#5)) are defined within the E. China domain based on anthropogenic NO_x

https://doi.org/10.5194/gmd-2023-35
Preprint. Discussion started: 4 April 2023
© Author(s) 2023. CC BY 4.0 License.

Geoscientific Model Development Discussions

82 emissions in 2015. Regions #1 and #2 are defined as highly polluted regions by excluding grids
83 with low and medium anthropogenic NO_x emissions. Tropospheric O_3 changes over these
84 regions are discussed to investigate the possible regional discrepancies in surface and free
85 tropospheric O_3 associated with different local pollution levels. Our conclusions follow in
86 Section 4.
87

88 ## 2. Data and Methods

89 ### 2.1 Surface O_3 measurements

90 We use MEE surface in situ O_3 concentration data (https://quotsoft.net/air/) for the period
91 2015-2020. These real-time monitoring stations have the ability to report hourly concentrations
92 of criteria pollutants from over 1650 sites in 2020. Concentrations were reported by the MEE
93 in ug m^{-3} under standard temperature (273 K) until 31 August 2018. This reference state was
94 changed on 1 September 2018 to 298 K. We converted the O_3 concentrations to ppb and
95 rescaled the post-August 2018 concentrations to the standard temperature (273 K) to maintain
96 consistency in the trend analysis. In addition, in situ hourly surface O_3 measurements from the
97 US AQS and European Environment Agency AirBase networks are used in the companion
98 paper (Part 2, Zhu et al. (2023)). The AQS and AirBase networks collect ambient air pollution
99 data from monitoring stations located in urban, suburban, and rural areas. We only considered
100 stations with at least 14 years of observation records in 2005-2020.

101 ### 2.2 OMI PROFOZ product

102 The OMI instrument was launched in July 2004 on the Aura spacecraft with a spatial
103 resolution of 13 × 24 km (nadir view). It provides global covered measurements with
104 backscattered sunlight in the ultraviolet–visible range from 270 to 500 nm (UV1: 270–310 nm;
105 UV2: 310–365 nm; visible: 350–500 nm). In this study, we use the OMI O_3 profile retrieval
106 product (PROFOZ v0.9.3, level 2, Liu et al., 2010; Huang et al., 2017) from the Smithsonian

https://doi.org/10.5194/gmd-2023-35
Preprint. Discussion started: 4 April 2023
© Author(s) 2023. CC BY 4.0 License.

Astrophysical Observatory (SAO). The retrieval uses the vector linearized discrete ordinate radiative transfer model (VLIDORT) (Spurr, 2006) and Bayesian optimal estimation. Profiles of partial O_3 columns (unit: DU) are retrieved in the spectral region 270–330 nm with 24 vertical layers: approximately 2.5 km for each layer from the surface to approximately 60 km.

The following filters are applied in our analysis following Huang et al. (2017): 1) nearly clear-sky scenes with effective cloud fraction < 0.3; 2) solar zenith angles (SZA) < 75°; and 3) fitting root mean square (RMS, ratio of fitting residuals to assumed measurement error) < 2.0. Starting in 2009, anomalies were found in OMI data and diagnosed as attenuated measured radiances in certain cross-track positions. This instrument degradation has been referred to as the "row anomaly". To enhance the quality and stability of data, only across-track positions between 4-11 (within 30 positions in the UV1 channels) are used in our analysis. This treatment is similar to the production of row-isolated data by using across-track positions between 3-18 (within 60 positions in the UV2 channels) in the OMI/MLS O_3 data (Ziemke et al., 2019; Wang et al., 2022).

The modeled tropospheric O_3 profiles in the assimilation processes and subsequent analyses are convolved by using the OMI retrieval averaging kernels and a priori O_3 profile based on the following equation:

$$\hat{\boldsymbol{x}} = \boldsymbol{x}_{\mathrm{a}} + \mathbf{A}(\boldsymbol{x} - \boldsymbol{x}_{\mathrm{a}}) \qquad \text{(Eq.1)}$$

where $\hat{\boldsymbol{x}}$ is the modeled O_3 profile convolved by the retrieval averaging kernels, $\boldsymbol{x}_a$ is the OMI a priori O_3 profile, $\boldsymbol{x}$ is the modeled O_3 profile, and $\mathbf{A}$ is the OMI averaging kernel matrix. Here $\mathrm{A(i,j)} = \frac{\partial \hat{x}_j}{\partial x_i}$, representing the sensitivity of the retrieved partial O_3 column (DU) at layer j to the change in O_3 (DU) at layer i. The unit for averaging kernels in this OMI product is DU/DU and does not cancel out because the conversion from DU to ppb varies with altitude.

2.3 GEOS-Chem model configuration

https://doi.org/10.5194/gmd-2023-35
Preprint. Discussion started: 4 April 2023
© Author(s) 2023. CC BY 4.0 License.

Geoscientific Model Development Discussions

The GEOS-Chem chemical transport model (http://www.geos-chem.org, version 12-8-1) is driven by assimilated meteorological data of MERRA-2. The GEOS-Chem full-chemistry simulation includes fully coupled O_3-NO_x-VOC-halogen-aerosol chemistry. Our analysis is conducted at a horizontal resolution of nested 0.5°×0.625° over China, the US and Europe with chemical boundary conditions archived every 3 hours from global simulations with 4°×5° resolution. Emissions are computed by the Harvard-NASA Emission Component (HEMCO). Global default anthropogenic emissions are from the CEDS (Community Emissions Data System) (Hoesly et al., 2018). Regional emissions are replaced by MEIC (Multiresolution Emission Inventory for China) in China, MIX in other regions of Asia (Li et al., 2017) and NEI2011 in the US. Open fire emissions are from the Global Fire Emissions Database (GFED4) (van der Werf et al., 2010).

Following Jiang et al. (2022), the total anthropogenic NO_x and VOC emissions in the GEOS-Chem model are scaled with the corresponding bottom-up inventories (MEIC for China, NEI2014 for the US, and ECLIPSE for Europe) so that the modeled surface nitrogen dioxide (NO_2) and O_3 concentrations in the a priori simulations are identical to Jiang et al. (2022) in 2005-2018. The total anthropogenic NO_x and VOC emissions in 2019-2020 in China, the US and Europe are further scaled based on linear projections. The total anthropogenic NO_x emissions in the a priori simulations declined by 53% (US) and 50% (Europe) in 2005-2020 and by 19% (China) in 2015-2020. The total anthropogenic VOC emissions in the a priori simulations declined by 19% (US) and 33% (Europe) in 2005-2020 and increased by 1% (China) in 2015-2020. We refer the reader to Jiang et al. (2022) for the details of the model configuration and performance, particularly the modeled trends of surface and tropospheric column NO_2 in 2005-2018.

2.4 Data assimilation approach

https://doi.org/10.5194/gmd-2023-35
Preprint. Discussion started: 4 April 2023
© Author(s) 2023. CC BY 4.0 License.

We employ the sequential KF to assimilate O_3 observations, which has been used in recent studies to optimize tropospheric CO concentrations (Tang et al., 2022; Han et al., 2022). As a brief description of the assimilation algorithm, the forward model (**M**) predicts the O_3 concentration ($\boldsymbol{x}_{\mathrm{at}}$) at time t:

$$\boldsymbol{x}_{\mathrm{at}} = \mathbf{M}_t \boldsymbol{x}_{t-1} \quad \text{(Eq. 2)}$$

The optimized O_3 concentrations can be expressed as:

$$\boldsymbol{x}_t = \boldsymbol{x}_{\mathrm{at}} + \mathbf{G}_t(\boldsymbol{y}_t - \mathbf{K}_t \boldsymbol{x}_{\mathrm{at}}) \quad \text{(Eq. 3)}$$

where $\boldsymbol{y}_t$ is the observation and $\mathbf{K}_t$ represents the operation operator that projects O_3 concentrations from the model space to the observation space. $\mathbf{G}_t$ is the KF gain matrix, which can be described as:

$$\mathbf{G}_t = \mathbf{S}_{\mathrm{at}} \mathbf{K}_t^T (\mathbf{K}_t \mathbf{S}_{\mathrm{at}} \mathbf{K}_t^T + \mathbf{S}_\epsilon)^{-1} \quad \text{(Eq. 4)}$$

where $\mathbf{S}_{\mathrm{at}}$ and $\mathbf{S}_\epsilon$ are the model and observation covariances, respectively. The optimized O_3 concentrations provided by Eq. 3 are then forwarded (hourly) to Eq. 2. The model errors are assumed to be 50%. The measurement errors are calculated as $\varepsilon_0 = ermax + 0.0075 * \Pi_0$, where *ermax* is the base error (1.5 μg m^{-3}) and Π_0 represents the observed O_3 concentrations (unit: μg m^{-3}). The representation errors are calculated as $\varepsilon_r = \gamma \varepsilon_0 \sqrt{\Delta l / L}$, where γ is a scaling factor (0.5), Δl is the model resolution (~56 km in this study), and L represents the range that the observation can reflect, which depends on the station type (2 km for urban, 4 km for suburban). The total observation error is then defined as $\varepsilon_t = \sqrt{\varepsilon_0^2 + \varepsilon_r^2}$. Following Tang et al. (2022), grid-based superobservations (0.5°×0.625°) were created to reduce the influence of representative errors.

3. Results and Discussion

3.1 GEOS-Chem tagged-O_3 simulation

A new chemical mechanism was developed in this work to allow the running of the single

https://doi.org/10.5194/gmd-2023-35
Preprint. Discussion started: 4 April 2023
© Author(s) 2023. CC BY 4.0 License.

Geoscientific Model Development Discussions

tracer tagged-O_3 mode. As shown in Fig. S1 (see the SI), the package of the Kinetic PreProcessor (KPP) module was modified to define the production (PO3) and loss (LO3) of O_3. The GEOS-Chem full-chemistry simulations with the updated KPP module were then performed to produce PO3 and LO3 every 20 minutes. Here the 20 minutes is selected to be the same as the chemical time step in GEOS-Chem full-chemistry mode to ensure consistency between tagged-O_3 and full chemistry simulations. Finally, the single tracer tagged-O_3 mode (tagged_o3_mod.F90) was performed by reading the archived PO3 and LO3 provided by the full-chemistry simulations. Because we are interested in tropospheric chemistry, we archived O_3 concentrations instead of O_3 production and loss rates in the stratosphere in the full chemistry simulations. The archived stratospheric O_3 concentrations were read in the tagged-O_3 simulation process as boundary conditions to ensure a reasonable stratospheric-tropospheric O_3 exchange.

Why is tagged-O_3 simulation useful if we must run the full-chemistry simulation first to produce PO3 and LO3? Table 1 shows the computation costs (hours of wall time per simulation year) by different GEOS-Chem simulation types in this work. We find 91%-94% reductions in the computation costs with respect to full-chemistry simulations: 57.5 and 5.2 hours at the global scale (4°×5°), 80.2 and 4.5 hours within the nested China domain (0.5°×0.625°), 160.7 and 9.4 hours within the nested US domain (0.5°×0.625°) and 103.4 and 6 hours within the nested Europe domain (0.5°×0.625°) by full chemistry and tagged-O_3 modes, respectively. Consequently, once the PO3 and LO3 are produced, the additional computational costs of performing tagged-O_3 simulation are almost negligible. The low computational costs of the tagged-O_3 simulation allow us to design and perform different assimilation experiments much more efficiently.

Here we evaluate the consistency in modeled O_3 concentrations between tagged-O_3 and full-chemistry simulations. Fig. 2A-E show the annual and seasonal averages of surface

https://doi.org/10.5194/gmd-2023-35
Preprint. Discussion started: 4 April 2023
© Author(s) 2023. CC BY 4.0 License.

Geoscientific Model Development Discussions

maximum daily 8-hour average (MDA8) O_3 over E. China in 2015-2020 from the full-chemistry simulation. The modeled surface MDA8 O_3 concentrations are as high as 60-70 ppb in the summer and as low as 10-20 ppb in the winter over northern China. The simulation with the tagged-O_3 mode (Fig. 2F-J) demonstrates spatial consistency with the full-chemistry simulation (Fig. 2A-E) and temporal consistency at both the daily (Fig. 3A) and monthly (Fig. 3B) scales in 2015-2020. In contrast, there are large discrepancies between full-chemistry (Fig. 2A-E) and tagged-O_x (Fig. 2K-O) simulations. As shown in Fig. 3, the O_x concentrations are higher than the O_3 concentrations by approximately 6 ppb, and the relative difference can reach 40% in the winter. Similarly, Fig. S2 (see the SI) shows the annual and seasonal averages of surface MDA8 O_3 over the US and Europe in 2005-2020 from the full-chemistry and tagged-O_3 simulations. Similar to China, we find good spatial (Fig. S2) and temporal (Fig. S3, see the SI) consistencies in surface MDA8 O_3 between tagged-O_3 and full-chemistry simulations over the US and Europe in 2005-2020. Our analysis thus indicates the reliability of the tagged-O_3 simulations developed in this work.

3.2 Surface O_3 by assimilating MEE O_3 observations

We first investigate the effects of surface O_3 observations on the tagged-O_3-based assimilations. O_3 at the surface level is formed by precursors mixed in the planetary boundary layer (PBL). Thus, it may not be accurate to assume that the differences between simulated and observed surface O_3 concentrations are completely caused by biased O_3 production and loss at the surface level. Here we adjust O_3 concentrations at all levels within the PBL when assimilating surface O_3 observations:

$$\Delta O_3^l = \Delta O_3^1 \times 0.8^{l-1} \quad \text{(Eq. 5)}$$

where ΔO_3^1 is the adjustment at the surface level calculated with Eq. 3; ΔO_3^l is the adjustment at model level *l*, which is based on ΔO_3^1 but decays exponentially with the increase in model level. We note that Eq. 5 is defined empirically, as we find that the assimilated O_3 matches

https://doi.org/10.5194/gmd-2023-35
Preprint. Discussion started: 4 April 2023
© Author(s) 2023. CC BY 4.0 License.

230 better with surface O_3 observations. More efforts are needed in the future to evaluate the
231 reliability of this empirical method.

232 Fig. 4A-E show the annual and seasonal averages of surface MDA8 O_3 observations from
233 MEE stations in 2015-2020. Fig. 4K-O further show the annual and seasonal averages of the a
234 posteriori O_3 concentrations by assimilating the MEE O_3 observations. As shown in Fig. 5, the
235 assimilated O_3 concentrations (blue lines) show good agreements with MEE O_3 observations
236 (red lines): the mean surface MDA8 O_3 in 2015-2020 are 42.9, 41.8 and 42.1 ppb (E. China),
237 42.3, 45.6 and 47.6 ppb (North China Plain), 44.5, 45.0 and 44.9 ppb (Yangtze River Delta),
238 44.7, 43.1 and 43.5 ppb (Central China), 45.3, 37.5 and 36.9 ppb (Sichuan Basin), and 43.0,
239 39.2 and 38.3 ppb (Southern China) in the a priori simulations, a posteriori simulations and
240 MEE observations, respectively. As we expected, MDA8 O_3 concentrations are higher over
241 areas with higher anthropogenic NO_x emissions, for example, 45.6 and 45.0 ppb in the North
242 China Plain and Yangtze River Delta, respectively, in contrast to 43.1, 37.5 and 39.2 ppb in
243 Central China, Sichuan Basin and Southern China, respectively.

244 As shown in Fig. 5A, there are good agreements between the a priori and a posteriori O_3
245 concentrations over E. China except a larger difference in the summer. However, as shown in
246 Fig. 4P-T, the good agreements between the a priori and a posteriori O_3 concentrations are
247 caused by the counterbalance of positive biases (i.e., overestimated surface O_3 in the a priori
248 simulations over southern China) and negative biases (i.e., underestimated surface O_3 in the a
249 priori simulations over northern China). The good agreements in Fig. 5A thus cannot represent
250 good performance in the simulations of surface O_3 concentrations. Furthermore, surface O_3
251 concentrations are maximum in June in the North China Plain, May and August in the Yangtze
252 River Delta, Central China and Sichuan Basin, September-October in Southern China (Fig. 5).
253 The assimilations exhibit noticeable declines in surface O_3 concentrations over regions #2-5 in
254 June-July, and the declines are underestimated by the a priori simulations. The inaccurate

https://doi.org/10.5194/gmd-2023-35
Preprint. Discussion started: 4 April 2023
© Author(s) 2023. CC BY 4.0 License.

Geoscientific Model Development Discussions

simulations of surface O_3 concentrations in June-July thus result in overestimated surface O_3 concentrations in the summer.

3.3 Rapid increasing trends in surface O_3 concentrations

Here we further investigate the changes in surface O_3 concentrations from observations and assimilations. As shown in Fig. 6F-J, the a priori simulation suggests slightly increasing trends of MDA8 O_3 in 2015-2020: 0.27 (spring), -0.23 (summer), 0.41 (autumn) and 0.40 (winter) ppb yr^{-1}, and the relative increasing trends are 0.6 (spring), -0.4 (summer), 1.0 (autumn) and 1.4 (winter) % yr^{-1}. The a priori simulation suggests increasing trends of surface O_3 concentrations in the summer over areas with higher local pollution levels, for example, 0.61 and 0.58 ppb yr^{-1} over the North China Plain and Yangtze River Delta, respectively, and decreasing trends of surface O_3 concentrations in the summer over areas with lower local pollution levels, for example, -0.10, -1.01 and -1.06 ppb yr^{-1} over Central China, Sichuan Basin and Southern China, respectively. The decreasing trends over areas with lower local pollution levels in the simulations are not surprising, given the decreases in anthropogenic NO_x emissions (Zheng et al., 2018; Jiang et al., 2022) and the reported NO_x-limited O_3 nonlinear chemical regimes in model simulations (Chen et al., 2021; Liu et al., 2021).

In contrast, the increasing trends in surface O_3 are much stronger in the assimilations. As shown in Table 2.1, our assimilation suggests 1.60 (spring), 1.16 (summer), 1.47 (autumn) and 0.80 (winter) ppb yr^{-1} increases in surface O_3 over E. China in 2015-2020, and the relative increasing trends are 3.4 (spring), 2.2 (summer), 3.7 (autumn) and 2.7 (winter) % yr^{-1}. The increasing trends are weaker when the modeled surface O_3 concentrations are averaged over E. China (Table 2.2) instead of sampling at the locations and times of MEE observations: 0.71 (spring), 0.36 (summer), 0.69 (autumn) and 0.54 (winter) ppb yr^{-1} because most MEE stations are urban sites. Our analysis thus indicates a noticeable underestimation in the increasing trends of surface O_3 concentrations in China in the a priori simulations, particularly in the summer,

https://doi.org/10.5194/gmd-2023-35
Preprint. Discussion started: 4 April 2023
© Author(s) 2023. CC BY 4.0 License.

Geoscientific Model Development Discussions

despite the anthropogenic NO_x and VOC emissions having been scaled in the simulations following Jiang et al. (2022).

The changes in surface O_3 concentrations have significant regional and seasonal discrepancies. As shown in Tables S1-S5 (see the SI), our assimilations demonstrate strong increasing trends in surface O_3 concentrations in 2015-2020 in the spring (1.94 ppb yr^{-1} or 3.8% yr^{-1}) and summer (2.52 ppb yr^{-1} or 4.0% yr^{-1}) over the North China Plain; in the spring (2.21 ppb yr^{-1} or 4.4% yr^{-1}) and autumn (1.84 ppb yr^{-1} or 4.1% yr^{-1}) over the Yangtze River Delta; in the spring (2.07 ppb yr^{-1} or 4.3% yr^{-1}) and autumn (2.09 ppb yr^{-1} or 4.7% yr^{-1}) over Central China; in the spring (1.69 ppb yr^{-1} or 3.8% yr^{-1}) over the Sichuan Basin; and in the autumn (2.21 ppb yr^{-1} or 4.9% yr^{-1}) over Southern China. While surface O_3 concentrations are higher over areas with higher anthropogenic NO_x emissions, the increasing trends in surface O_3 concentrations over Central China and Southern China are comparable with those in the North China Plain and Yangtze River Delta. Our analysis advises more attention to O_3 pollution in spring and autumn over areas with lower anthropogenic NO_x emissions because of the rapid increases in surface O_3 concentrations.

3.4 Tropospheric O_3 columns by assimilating OMI O_3 observations

Fig. 7A-E show the annual and seasonal averages of tropospheric OMI O_3 columns in 2015-2020. OMI is sensitive to O_3 at different vertical levels (Huang et al., 2017; Fu et al., 2018), and thus, the standard KF algorithm (Eq. 3) was employed to adjust tropospheric O_3 vertical profiles with the application of OMI O_3 averaging kernels. Fig. 7K-O show the annual and seasonal averages of the a posteriori tropospheric O_3 columns by assimilating OMI O_3 observations. The assimilated tropospheric O_3 columns show good agreement with OMI O_3 observations: the mean tropospheric O_3 columns in 2015-2020 (Table 2.3) are 37.1 DU in the a priori simulations, and 37.9 and 38.0 DU in the a posteriori simulation and OMI observations, respectively. Furthermore, as shown in Fig. 8, the trends of tropospheric O_3 columns in 2015-

https://doi.org/10.5194/gmd-2023-35
Preprint. Discussion started: 4 April 2023
© Author(s) 2023. CC BY 4.0 License.

Geoscientific Model Development Discussions

2020 (Table 2.3) are 0.02 DU yr^{-1} in the a priori simulations, and -0.17 and -0.30 DU yr^{-1} in the a posteriori simulation and OMI observations, respectively.

The discrepancies between the a priori and a posteriori tropospheric O_3 columns by assimilating OMI O_3 observations (Fig. 7) are smaller than those in surface O_3 concentrations (Fig. 4). A better simulation capability in tropospheric column O_3 is expected because model simulation with 0.5°×0.625° horizontal resolution may not be enough to accurately resolve O_3 nonlinear chemical regimes over urban surface stations. Furthermore, in contrast to the wide distributions of increasing trends of O_3 at the surface level (Fig. 6), both OMI O_3 observations (-0.30 DU yr^{-1}) and the OMI-based assimilations (-0.17 DU yr^{-1}) suggest decreasing trends in tropospheric O_3 columns over E. Asia in 2015-2020 (Fig. 8). The decreasing trends are stronger in the summer and weaker in the spring. However, the trends shown in Fig. 8 may not represent the actual tropospheric O_3 changes well because the convolution of OMI O_3 averaging kernels on the output O_3 profiles can affect the weights of the derived tropospheric columns to O_3 at different vertical levels.

Consequently, Fig. 9 further shows the annual and seasonal averages of tropospheric O_3 columns from a priori and a posteriori simulations, in which the output O_3 profiles are not convolved with OMI retrieval averaging kernels so that they can better represent the actual atmospheric O_3 state. As shown in Fig. 10, the assimilated tropospheric O_3 columns are 37.2 and 38.8 DU (E. China), 41.4 and 43.7 DU (North China Plain), 46.0 and 48.1 DU (Yangtze River Delta), 45.9 and 48.1 DU (Central China), 42.6 and 44.6 DU (Sichuan Basin), 38.8 and 40.6 DU (Southern China) in 2015-2020 by assimilating MEE and OMI O_3 observations, respectively. In contrast to the higher surface MDA8 O_3 concentrations over areas with higher anthropogenic NO_x emissions, tropospheric O_3 columns over Central China and the Sichuan Basin are even higher than those over the highly polluted North China Plain. In addition, tropospheric O_3 columns by assimilating MEE surface O_3 observations are lower than those by

https://doi.org/10.5194/gmd-2023-35
Preprint. Discussion started: 4 April 2023
© Author(s) 2023. CC BY 4.0 License.

assimilating OMI O_3 observations, and their difference is larger in the summer and smaller in the winter.

The assimilated tropospheric O_3 columns are maximum in June-July in North China Plain (Fig. 10). However, the assimilated tropospheric O_3 columns are maximum in March-May over other regions that are dramatically different with surface O_3 (Fig. 5). The similar seasonality between surface and free tropospheric O_3 over highly polluted North China Plain reflects the impact of local emissions. The different seasonality over other regions may represent the contributions from free tropospheric O_3 transport. While the Yangtze River Delta is defined as a highly polluted region, its area is much smaller than North China Plain (Fig. 1) and thus the impact of local emissions on tropospheric O_3 columns over the Yangtze River Delta may not be as strong as the North China Plain. Furthermore, as shown in Fig. 11, the impacts of different surface and satellite O_3 observations on the assimilated O_3 vertical profiles are limited. The assimilation of MEE surface O_3 observations leads to decreases in O_3 concentrations in the lower troposphere from the surface to 600 hPa levels over the Sichuan Basin and Southern China; the assimilation of OMI O_3 observations leads to enhancement in O_3 concentrations in the middle and upper troposphere over the highly polluted North China Plain.

As shown in Fig. 12, the trends of tropospheric O_3 columns in 2015-2020 are 0.06, 0.25 and -0.10 DU yr^{-1} (E. China), 0.26, 0.66 and 0.12 DU yr^{-1} (North China Plain), 0.28, 0.60 and 0.13 DU yr^{-1} (Yangtze River Delta), 0.09, 0.46 and -0.06 DU yr^{-1} (Central China), -0.14, 0.17 and -0.29 DU yr^{-1} (Sichuan Basin), -0.08, 0.15 and -0.25 DU yr^{-1} (Southern China) in the a priori simulations and a posteriori simulations by assimilating MEE and OMI O_3 observations, respectively. The higher positive trends by assimilating MEE observations are expected, given the increasing trends in surface O_3 concentrations (1.77 ppb yr^{-1}) and decreasing trends in OMI O_3 concentrations (-0.30 DU yr^{-1}) over E. China. The stronger increasing trends in free tropospheric O_3 over the highly polluted North China Plain and Yangtze River Delta may

https://doi.org/10.5194/gmd-2023-35
Preprint. Discussion started: 4 April 2023
© Author(s) 2023. CC BY 4.0 License.

Geoscientific Model Development Discussions

reflect the larger contributions of local emissions to tropospheric O_3 columns over highly polluted areas, and the increasing trends are stronger in autumn and winter. The large discrepancy between assimilations by assimilating surface and satellite observations further indicates the possible uncertainties in the derived free tropospheric O_3 changes. Assimilations of both surface and satellite observations, as shown in this work, are thus expected to provide more information to better describe the changes in free tropospheric O_3.

4. Conclusion

The single tracer tagged-O_3 mode was developed in this work to build the capability of the GEOS-Chem model for rapid simulations of tropospheric O_3. The tagged-O_3 mode demonstrates high consistency with GEOS-Chem full-chemistry simulation. In contrast, the O_x concentrations provided by the tagged-O_x mode are higher than the O_3 concentrations by approximately 6 ppb, and the relative difference can reach 40% in the winter. The computational costs of the tagged-O_3 mode are reduced by approximately 91-94% with respect to the full-chemistry mode. For example, the computational costs (hours of wall time per simulation year) are 57.5 and 5.2 hours at the global scale (4°×5°), 80.2 and 4.5 hours within the nested China domain (0.5°×0.625°), 160.7 and 9.4 hours within the nested US domain (0.5°×0.625°) and 103.4 and 6 hours within the nested Europe domain (0.5°×0.625°) by full chemistry and tagged-O_3 simulations, respectively. The low computational costs of the tagged-O_3 simulation thus allow us to design and perform different assimilation experiments much more efficiently.

The tagged-O_3 simulation was combined with MEE and OMI O_3 observations to investigate the changes in tropospheric O_3 over E. Asia in 2015-2020. The assimilated O_3 concentrations demonstrate good agreement with O_3 observations: surface O_3 concentrations are 42.9, 41.8 and 42.1 ppb over E. China in a priori and a posteriori simulations and MEE O_3 observations, respectively; tropospheric O_3 columns are 37.1, 37.9 and 38.0 DU over E. China

https://doi.org/10.5194/gmd-2023-35
Preprint. Discussion started: 4 April 2023
© Author(s) 2023. CC BY 4.0 License.

in a priori and a posteriori simulations (convolved with OMI retrieval averaging kernels) and OMI O_3 observations, respectively. We find noticeable biases in modeled surface O_3 concentrations, for example, overestimated surface O_3 over southern China and underestimated surface O_3 over northern China. The assimilations indicate rapidly increasing trends of surface O_3 concentrations by 1.60 (spring), 1.16 (summer), 1.47 (autumn) and 0.80 (winter) ppb yr^{-1} over E. China in 2015-2020, and the increasing trends are underestimated by the a priori simulations. While surface O_3 concentrations are higher over areas with higher anthropogenic NO_x emissions, we find that the increasing trends in surface O_3 concentrations over Central China and Southern China are comparable with those in the North China Plain and Yangtze River Delta. Our analysis thus advises more attention to O_3 pollution in spring and autumn over areas with lower anthropogenic NO_x emissions because of the rapid increases in surface O_3 concentrations.

Furthermore, the trends in assimilated tropospheric O_3 columns in 2015-2020 are 0.25 and -0.10 DU yr^{-1} (E. China), 0.66 and 0.12 DU yr^{-1} (North China Plain), 0.60 and 0.13 DU yr^{-1} (Yangtze River Delta), 0.46 and -0.06 DU yr^{-1} (Central China), 0.17 and -0.29 DU yr^{-1} (Sichuan Basin), 0.15 and -0.25 DU yr^{-1} (Southern China) by assimilating MEE surface and OMI O_3 observations, respectively. The stronger increasing trends in tropospheric O_3 columns over the highly polluted North China Plain and Yangtze River Delta may reflect the larger contributions of local emissions to tropospheric O_3 columns over highly polluted areas. The large discrepancy between assimilations by assimilating surface and satellite observations further indicates the possible uncertainties in the derived free tropospheric O_3 changes. This work demonstrates the importance of data assimilation techniques to provide extension and interpretation of O_3 observations.

https://doi.org/10.5194/gmd-2023-35
Preprint. Discussion started: 4 April 2023
© Author(s) 2023. CC BY 4.0 License.

Geoscientific Model Development Discussions

Code and data availability: The MEE O_3 data can be downloaded from https://quotsoft.net/air/. The AQS and AirBase surface O_3 data can be downloaded from https://www.eea.europa.eu/data-and-maps/data/aqereporting-8 and https://aqs.epa.gov/aqsweb/airdata/download_files.html#Row. The OMI PROFOZ product can be acquired at https://avdc.gsfc.nasa.gov/pub/data/satellite/Aura/OMI/V03/L2/OMPROFOZ/. The GEOS-Chem model (version 12.8.1) can be downloaded from http://wiki.seas.harvard.edu/geos-chem/index.php/GEOS-Chem_12#12.8.1. The KPP module for tagged-O_3 simulations can be downloaded from https://doi.org/10.5281/zenodo.7545944.

Author Contributions: Z.J. designed the research. R.Z. developed the model code and performed the research. Z.J. and R.Z. wrote the manuscript. X.L. provided instruction for the usage of OMI data. All authors contributed to discussions and editing the manuscript.

Competing interests: The contact author has declared that neither they nor their co-authors have any competing interests.

Acknowledgments: We thank the China Ministry of Ecology and Environment (MEE), the United States Environmental Protection Agency and the European Environmental Agency for providing the surface O_3 measurements. The numerical calculations in this paper have been done on the supercomputing system in the Supercomputing Center of University of Science and Technology of China. This work was supported by the Hundred Talents Program of Chinese Academy of Science and National Natural Science Foundation of China (42277082, 41721002).

Table and Figures

Table 1. Computation costs (hours of wall time) by different GEOS-Chem simulation types.

https://doi.org/10.5194/gmd-2023-35
Preprint. Discussion started: 4 April 2023
© Author(s) 2023. CC BY 4.0 License.

Table 2. Averages (with units ppb or DU) and trends (with units ppb yr^{-1} or DU yr^{-1}) of surface and tropospheric column O_3 concentrations in 2015-2020 over E. China from observations (MEE and OMI) and a priori and a posteriori (KF) simulations. T2.1): the modeled surface O_3 is sampled at the locations and times of MEE surface O_3 observations; T2.2): the modeled surface O_3 is averaged over E. China (land only); T2.3): the output O_3 profiles from the a priori and a posteriori simulations are convolved with OMI O_3 averaging kernels; T2.4): the output O_3 profiles are NOT convolved with OMI O_3 averaging kernels.

Fig. 1. (a) Anthropogenic NO_x emissions over E. China in 2015; (b) Region definitions for the North China Plain (#1), Yangtze River Delta (#2), Central China (#3), Sichuan Basin (#4) and Southern China (#5). The different colors (red, gray and green) represent grids with high (highest 15%), medium (15-50%) and low (lowest 50%) anthropogenic NO_x emissions. Regions #1 and #2 are defined as highly polluted (HP) regions by excluding grids with low and medium anthropogenic NO_x emissions.

Fig. 2. Surface MDA8 O_3 in 2015-2020 (annual and seasonal averages) simulated by GEOS-Chem model with (A-E) full chemistry mode; (F-J) tagged-O_3 mode; and (K-O) tagged-O_x mode. The 8-hour range of surface O_x is selected according to the time range of MDA8 O_3.

Fig. 3. (A) Daily averages of surface MDA8 O_3 over E. China in 2015-2020 from GEOS-Chem full chemistry (black), tagged-O_3 (blue) and tagged-O_x (red) simulations; (B) Monthly averages of MDA8 O_3. The dashed lines in panel B are annual averages.

Fig. 4. Surface MDA8 O_3 in 2015-2020 (annual and seasonal averages) from (A-E) MEE stations; (F-J) GEOS-Chem a priori simulation; (K-O) GEOS-Chem a posteriori simulation by assimilating MEE O_3 observations. (P-T) bias in the a priori simulations calculated by a posteriori minus a priori O_3 concentrations.

Fig. 5. (A-F) Daily averages of surface MDA8 O_3 in 2015-2020 from MEE stations (red) and GEOS-Chem a priori (black) and a posteriori (blue) simulations by assimilating MEE O_3 observations. (G-L) Monthly averages of MDA8 O_3. The dashed lines in panels G-L are annual averages.

https://doi.org/10.5194/gmd-2023-35
Preprint. Discussion started: 4 April 2023
© Author(s) 2023. CC BY 4.0 License.

Fig. 6. Trends of surface MDA8 O_3 in 2015-2020 (annual and seasonal averages) from (A-E) MEE stations; (F-J) GEOS-Chem a priori simulation; (K-O) GEOS-Chem a posteriori simulation by assimilating MEE O_3 observations.

Fig. 7. Tropospheric O_3 columns in 2015-2020 (annual and seasonal averages) from (A-E) OMI observations; (F-J) GEOS-Chem a priori simulation; (K-O) GEOS-Chem a posteriori simulation by assimilating OMI O_3 observations. (P-T) bias in the a priori simulations calculated by a posteriori minus a priori tropospheric O_3 columns. The output O_3 profiles are convolved with OMI averaging kernels.

Fig. 8. Trends of tropospheric O_3 columns in 2015-2020 (annual and seasonal averages) from (A-E) OMI observations; (F-J) GEOS-Chem a priori simulation; (K-O) GEOS-Chem a posteriori simulation by assimilating OMI O_3 observations. The output O_3 profiles are convolved with OMI averaging kernels.

Fig. 9. Tropospheric O_3 columns in 2015-2020 (annual and seasonal averages) from (A-E) GEOS-Chem a priori simulation; (F-J) assimilations of MEE surface O_3 observations; (K-O) assimilations of OMI O_3 observations. (P-T) difference in tropospheric O_3 columns calculated by OMI-based assimilations minus MEE-based assimilations.

Fig. 10. (A-F) Daily averages of tropospheric O_3 columns in 2015-2020 from GEOS-Chem a priori simulation (black) and a posteriori simulations by assimilating MEE (blue) and OMI (red) O_3 observations. (G-L) Monthly averages of tropospheric O_3 columns. The dashed lines in panels G-L are annual averages.

Fig. 11. Averages of O_3 vertical profiles in 2015-2020 from GEOS-Chem a priori (black) and a posteriori simulations by assimilating MEE (blue) and OMI (red) O_3 observations.

Fig. 12. Trends of tropospheric O_3 columns in 2015-2020 (annual and seasonal averages) from (A-E) GEOS-Chem a priori simulation; (F-J) assimilations of MEE surface O_3 observations; (K-O) assimilations of OMI O_3 observations.

References

https://doi.org/10.5194/gmd-2023-35
Preprint. Discussion started: 4 April 2023
© Author(s) 2023. CC BY 4.0 License.

497 Chen, J., Jiang, Z., Li, R., Liao, C., Miyazaki, K., and Jones, D. B. A.: Large discrepancy
498 between observed and modeled wintertime tropospheric NO_2 variabilities due to COVID-19
499 controls in China, Environ Res Let, 17, 035007, 10.1088/1748-9326/ac4ec0, 2022.
500 Chen, X., Jiang, Z., Shen, Y., Li, R., Fu, Y., Liu, J., Han, H., Liao, H., Cheng, X., Jones, D. B.
501 A., Worden, H., and Abad, G. G.: Chinese Regulations Are Working—Why Is Surface Ozone
502 Over Industrialized Areas Still High? Applying Lessons From Northeast US Air Quality
503 Evolution, Geophys Res Lett, 48, e2021GL092816, 10.1029/2021gl092816, 2021.
504 Colombi, N., Miyazaki, K., Bowman, K. W., Neu, J. L., and Jacob, D. J.: A new methodology
505 for inferring surface ozone from multispectral satellite measurements, Environ Res Let, 16,
506 105005, 10.1088/1748-9326/ac243d, 2021.
507 Elguindi, N., Granier, C., Stavrakou, T., Darras, S., Bauwens, M., Cao, H., Chen, C., Denier
508 van der Gon, H. A. C., Dubovik, O., Fu, T. M., Henze, D. K., Jiang, Z., Keita, S., Kuenen, J.
509 J. P., Kurokawa, J., Liousse, C., Miyazaki, K., Müller, J. F., Qu, Z., Solmon, F., and Zheng,
510 B.: Intercomparison of Magnitudes and Trends in Anthropogenic Surface Emissions From
511 Bottom‐Up Inventories, Top‐Down Estimates, and Emission Scenarios, Earth's Future, 8,
512 e2020EF001520, 10.1029/2020ef001520, 2020.
513 Fu, D., Kulawik, S. S., Miyazaki, K., Bowman, K. W., Worden, J. R., Eldering, A., Livesey,
514 N. J., Teixeira, J., Irion, F. W., Herman, R. L., Osterman, G. B., Liu, X., Levelt, P. F.,
515 Thompson, A. M., and Luo, M.: Retrievals of tropospheric ozone profiles from the synergism
516 of AIRS and OMI: methodology and validation, Atmos Meas Tech, 11, 5587-5605,
517 10.5194/amt-11-5587-2018, 2018.
518 Han, H., Liu, J., Yuan, H., Zhuang, B., Zhu, Y., Wu, Y., Yan, Y., and Ding, A.: Characteristics
519 of intercontinental transport of tropospheric ozone from Africa to Asia, Atmos Chem Phys,
520 18, 4251-4276, 10.5194/acp-18-4251-2018, 2018.
521 Han, W., He, T.-L., Tang, Z., Wang, M., Jones, D., and Jiang, Z.: A comparative analysis for
522 a deep learning model (hyDL-CO v1.0) and Kalman filter to predict CO concentrations in
523 China, Geosci Model Dev, 15, 4225-4237, 10.5194/gmd-15-4225-2022, 2022.
524 Hoesly, R. M., Smith, S. J., Feng, L., Klimont, Z., Janssens-Maenhout, G., Pitkanen, T.,
525 Seibert, J. J., Vu, L., Andres, R. J., Bolt, R. M., Bond, T. C., Dawidowski, L., Kholod, N.,
526 Kurokawa, J.-i., Li, M., Liu, L., Lu, Z., Moura, M. C. P., O'Rourke, P. R., and Zhang, Q.:
527 Historical (1750–2014) anthropogenic emissions of reactive gases and aerosols from the
528 Community Emissions Data System (CEDS), Geosci Model Dev, 11, 369-408, 10.5194/gmd-
529 11-369-2018, 2018.
530 Huang, G., Liu, X., Chance, K., Yang, K., Bhartia, P. K., Cai, Z., Allaart, M., Ancellet, G.,
531 Calpini, B., Coetzee, G. J. R., Cuevas-Agulló, E., Cupeiro, M., De Backer, H., Dubey, M. K.,
532 Fuelberg, H. E., Fujiwara, M., Godin-Beekmann, S., Hall, T. J., Johnson, B., Joseph, E., Kivi,
533 R., Kois, B., Komala, N., König-Langlo, G., Laneve, G., Leblanc, T., Marchand, M.,
534 Minschwaner, K. R., Morris, G., Newchurch, M. J., Ogino, S.-Y., Ohkawara, N., Piters, A. J.
535 M., Posny, F., Querel, R., Scheele, R., Schmidlin, F. J., Schnell, R. C., Schrems, O., Selkirk,
536 H., Shiotani, M., Skrivánková, P., Stübi, R., Taha, G., Tarasick, D. W., Thompson, A. M.,
537 Thouret, V., Tully, M. B., Van Malderen, R., Vömel, H., von der Gathen, P., Witte, J. C., and
538 Yela, M.: Validation of 10-year SAO OMI Ozone Profile (PROFOZ) product using

https://doi.org/10.5194/gmd-2023-35
Preprint. Discussion started: 4 April 2023
© Author(s) 2023. CC BY 4.0 License.

ozonesonde observations, Atmos Meas Tech, 10, 2455-2475, 10.5194/amt-10-2455-2017, 2017.

Huijnen, V., Miyazaki, K., Flemming, J., Inness, A., Sekiya, T., and Schultz, M. G.: An intercomparison of tropospheric ozone reanalysis products from CAMS, CAMS interim, TCR-1, and TCR-2, Geosci Model Dev, 13, 1513-1544, 10.5194/gmd-13-1513-2020, 2020.

Jiang, Z., Worden, J. R., Jones, D. B. A., Lin, J. T., Verstraeten, W. W., and Henze, D. K.: Constraints on Asian ozone using Aura TES, OMI and Terra MOPITT, Atmos Chem Phys, 15, 99-112, 10.5194/acp-15-99-2015, 2015.

Jiang, Z., Zhu, R., Miyazaki, K., McDonald, B. C., Klimont, Z., Zheng, B., Boersma, K. F., Zhang, Q., Worden, H., Worden, J. R., Henze, D. K., Jones, D. B. A., Denier van der Gon, H. A. C., and Eskes, H.: Decadal Variabilities in Tropospheric Nitrogen Oxides Over United States, Europe, and China, J Geophys Res-Atmos, 127, e2021JD035872, 10.1029/2021jd035872, 2022.

Li, D., Shindell, D., Ding, D., Lu, X., Zhang, L., and Zhang, Y.: Surface ozone impacts on major crop production in China from 2010 to 2017, Atmos Chem Phys, 22, 2625-2638, 10.5194/acp-22-2625-2022, 2022.

Li, M., Zhang, Q., Kurokawa, J.-i., Woo, J.-H., He, K., Lu, Z., Ohara, T., Song, Y., Streets, D. G., Carmichael, G. R., Cheng, Y., Hong, C., Huo, H., Jiang, X., Kang, S., Liu, F., Su, H., and Zheng, B.: MIX: a mosaic Asian anthropogenic emission inventory under the international collaboration framework of the MICS-Asia and HTAP, Atmos Chem Phys, 17, 935-963, 10.5194/acp-17-935-2017, 2017.

Liu, Z., Doherty, R. M., Wild, O., Hollaway, M., and O'Connor, F. M.: Contrasting chemical environments in summertime for atmospheric ozone across major Chinese industrial regions: the effectiveness of emission control strategies, Atmos Chem Phys, 21, 10689-10706, 10.5194/acp-21-10689-2021, 2021.

Ma, C., Wang, T., Mizzi, A. P., Anderson, J. L., Zhuang, B., Xie, M., and Wu, R.: Multiconstituent Data Assimilation With WRF‐Chem/DART: Potential for Adjusting Anthropogenic Emissions and Improving Air Quality Forecasts Over Eastern China, J Geophys Res-Atmos, 7393‐7412, 10.1029/2019jd030421, 2019.

Miyazaki, K., Bowman, K. W., Yumimoto, K., Walker, T., and Sudo, K.: Evaluation of a multi-model, multi-constituent assimilation framework for tropospheric chemical reanalysis, Atmos Chem Phys, 20, 931-967, 10.5194/acp-20-931-2020, 2020.

Peng, X., Wang, W., Xia, M., Chen, H., Ravishankara, A. R., Li, Q., Saiz-Lopez, A., Liu, P., Zhang, F., Zhang, C., Xue, L., Wang, X., George, C., Wang, J., Mu, Y., Chen, J., and Wang, T.: An unexpected large continental source of reactive bromine and chlorine with significant impact on wintertime air quality, Natl Sci Rev, 8, nwaa304, 10.1093/nsr/nwaa304, 2021.

Peng, Z., Lei, L., Liu, Z., Sun, J., Ding, A., Ban, J., Chen, D., Kou, X., and Chu, K.: The impact of multi-species surface chemical observation assimilation on air quality forecasts in China, Atmos Chem Phys, 18, 17387-17404, 10.5194/acp-18-17387-2018, 2018.

Spurr, R. J. D.: VLIDORT: A linearized pseudo-spherical vector discrete ordinate radiative transfer code for forward model and retrieval studies in multilayer multiple scattering media,

https://doi.org/10.5194/gmd-2023-35
Preprint. Discussion started: 4 April 2023
© Author(s) 2023. CC BY 4.0 License.

580 Journal of Quantitative Spectroscopy and Radiative Transfer, 102, 316-342,
581 10.1016/j.jqsrt.2006.05.005, 2006.
582 Tang, Z., Chen, J., and Jiang, Z.: Discrepancy in assimilated atmospheric CO over East Asia
583 in 2015–2020 by assimilating satellite and surface CO measurements, Atmos Chem Phys, 22,
584 7815-7826, 10.5194/acp-22-7815-2022, 2022.
585 van der Werf, G. R., Randerson, J. T., Giglio, L., Collatz, G. J., Mu, M., Kasibhatla, P. S.,
586 Morton, D. C., DeFries, R. S., Jin, Y., and van Leeuwen, T. T.: Global fire emissions and the
587 contribution of deforestation, savanna, forest, agricultural, and peat fires (1997–2009), Atmos
588 Chem Phys, 10, 11707-11735, 10.5194/acp-10-11707-2010, 2010.
589 van Peet, J. C. A., van der A, R. J., Kelder, H. M., and Levelt, P. F.: Simultaneous assimilation
590 of ozone profiles from multiple UV-VIS satellite instruments, Atmos Chem Phys, 18, 1685-
591 1704, 10.5194/acp-18-1685-2018, 2018.
592 Wang, X., Fu, T. M., Zhang, L., Lu, X., Liu, X., Amnuaylojaroen, T., Latif, M. T., Ma, Y.,
593 Zhang, L., Feng, X., Zhu, L., Shen, H., and Yang, X.: Rapidly Changing Emissions Drove
594 Substantial Surface and Tropospheric Ozone Increases Over Southeast Asia, Geophys Res
595 Lett, 49, e2022GL100223, 10.1029/2022gl100223, 2022.
596 Xue, L., Ding, A., Cooper, O., Huang, X., Wang, W., Zhou, D., Wu, Z., McClure-Begley, A.,
597 Petropavlovskikh, I., Andreae, M. O., and Fu, C.: ENSO and Southeast Asian biomass
598 burning modulate subtropical trans-Pacific ozone transport, Natl Sci Rev, 8, nwaa132,
599 10.1093/nsr/nwaa132, 2021.
600 Zhang, L., Jacob, D. J., Boersma, K. F., Jaffe, D. A., Olson, J. R., Bowman, K. W., Worden, J.
601 R., Thompson, A. M., Avery, M. A., Cohen, R. C., Dibb, J. E., Flock, F. M., Fuelberg, H. E.,
602 Huey, L. G., McMillan, W. W., Singh, H. B., and Weinheimer, A. J.: Transpacific transport
603 of ozone pollution and the effect of recent Asian emission increases on air quality in North
604 America: an integrated analysis using satellite, aircraft, ozonesonde, and surface
605 observations, Atmos Chem Phys, 8, 6117-6136, DOI 10.5194/acp-8-6117-2008, 2008.
606 Zhang, Y., Cooper, O. R., Gaudel, A., Nedelec, P., Ogino, S. Y., Thompson, A. M., and West,
607 J. J.: Tropospheric ozone change from 1980 to 2010 dominated by equatorward redistribution
608 of emissions, Nat Geosci, 9, 875-879, 10.1038/NGEO2827, 2016.
609 Zhang, Y., Shindell, D., Seltzer, K., Shen, L., Lamarque, J.-F., Zhang, Q., Zheng, B., Xing, J.,
610 Jiang, Z., and Zhang, L.: Impacts of emission changes in China from 2010 to 2017 on
611 domestic and intercontinental air quality and health effect, Atmos Chem Phys, 21, 16051-
612 16065, 10.5194/acp-21-16051-2021, 2021.
613 Zheng, B., Tong, D., Li, M., Liu, F., Hong, C., Geng, G., Li, H., Li, X., Peng, L., Qi, J., Yan,
614 L., Zhang, Y., Zhao, H., Zheng, Y., He, K., and Zhang, Q.: Trends in China's anthropogenic
615 emissions since 2010 as the consequence of clean air actions, Atmos Chem Phys, 18, 14095-
616 14111, 10.5194/acp-18-14095-2018, 2018.
617 Zhu, R., Tang, Z., Chen, X., Jiang, Z., and Liu, X.: Rapid assimilations of O_3 observations –
618 Part 2: tropospheric O_3 changes in in the United States and Europe in 2005-2020, submitted
619 to Atmos Chem Phys, 2023.
620 Zhu, Y., Liu, J., Wang, T., Zhuang, B., Han, H., Wang, H., Chang, Y., and Ding, K.: The
621 Impacts of Meteorology on the Seasonal and Interannual Variabilities of Ozone Transport

https://doi.org/10.5194/gmd-2023-35
Preprint. Discussion started: 4 April 2023
© Author(s) 2023. CC BY 4.0 License.

From North America to East Asia, J Geophys Res-Atmos, 122, 10,612-610,636, 10.1002/2017jd026761, 2017.

Ziemke, J. R., Oman, L. D., Strode, S. A., Douglass, A. R., Olsen, M. A., McPeters, R. D., Bhartia, P. K., Froidevaux, L., Labow, G. J., Witte, J. C., Thompson, A. M., Haffner, D. P., Kramarova, N. A., Frith, S. M., Huang, L.-K., Jaross, G. R., Seftor, C. J., Deland, M. T., and Taylor, S. L.: Trends in global tropospheric ozone inferred from a composite record of TOMS/OMI/MLS/OMPS satellite measurements and the MERRA-2 GMI simulation, Atmos Chem Phys, 19, 3257-3269, 10.5194/acp-19-3257-2019, 2019.

https://doi.org/10.5194/gmd-2023-35
Preprint. Discussion started: 4 April 2023
© Author(s) 2023. CC BY 4.0 License.

Geoscientific Model Development Discussions

Simulation Type	Region	Resolution	Domain Definition	Hours per Year	CPU Number
Full Chemistry (tropchem)	Global	4x5	90S-90N, 180W-180E	57.5	20
	China	0.5x0.625	17.5N-47.5N, 97.5E-127.5E	80.2	20
	United States	0.5x0.625	24.0N-54.0N, 130W-65W	160.7	20
	Europe	0.5x0.625	32.0N-62.0N, 15W-25E	103.4	20
tagged-O3	Global	4x5	90S-90N, 180W-180E	5.2	20
	China	0.5x0.625	17.5N-47.5N, 97.5E-127.5E	4.5	20
	United States	0.5x0.625	24.0N-54.0N, 130W-65W	9.4	20
	Europe	0.5x0.625	32.0N-62.0N, 15W-25E	6	20

Table. 1. Computation costs (hours of wall time) by different GEOS-Chem simulation types.

E. China (2015-2020)		Annual		Spring		Summer		Autumn		Winter	
		Mean	Trend	Mean	Trend	Mean	Trend	Mean	Trend	Mean	Trend
T2.1 surface (sampled)	MEE	42.1	1.77	48.4	2.25	51.7	1.70	39.8	2.01	29.6	1.14
	a priori	42.9	0.16	47.8	0.27	55.8	-0.23	39.9	0.41	28.5	0.40
	KF-MEE	41.8	1.24	47.2	1.60	51.7	1.16	39.5	1.47	29.5	0.80
T2.2 surface	a priori	42.3	0.05	47.5	0.12	52.4	-0.31	38.8	0.20	30.8	0.35
	KF-MEE	41.3	0.55	46.7	0.71	49.8	0.36	38.0	0.69	31.0	0.54
T2.3 trop. column (convolved)	OMI	38.0	-0.30	40.9	0.12	45.9	-0.66	34.6	-0.41	30.4	-0.48
	a priori	37.1	0.02	41.0	0.17	43.1	-0.21	32.6	0.15	31.3	-0.06
	KF-OMI	37.9	-0.17	41.1	0.08	45.5	-0.51	34.2	-0.17	30.7	-0.17
T2.4 trop. Column	a priori	38.2	0.06	42.8	-0.03	42.4	0.00	33.2	0.29	34.8	0.09
	KF-MEE	37.2	0.25	41.8	0.18	40.7	0.30	32.2	0.45	34.4	0.18
	KF-OMI	38.8	-0.10	42.9	-0.17	44.1	-0.22	34.4	0.04	34.2	-0.02

Table. 2. Averages (with units ppb or DU) and trends (with units ppb yr^{-1} or DU yr^{-1}) of surface and tropospheric column O_3 concentrations in 2015-2020 over E. China from observations (MEE and OMI) and a priori and a posteriori (KF) simulations. T2.1): the modeled surface O_3 is sampled at the locations and times of MEE surface O_3 observations; T2.2): the modeled surface O_3 is averaged over E. China (land only); T2.3): the output O_3 profiles from the a priori and a posteriori simulations are convolved with OMI O_3 averaging kernels; T2.4): the output O_3 profiles are NOT convolved with OMI O_3 averaging kernels.

https://doi.org/10.5194/gmd-2023-35
Preprint. Discussion started: 4 April 2023
© Author(s) 2023. CC BY 4.0 License.

Geoscientific Model Development
Discussions
Open Access
EGU

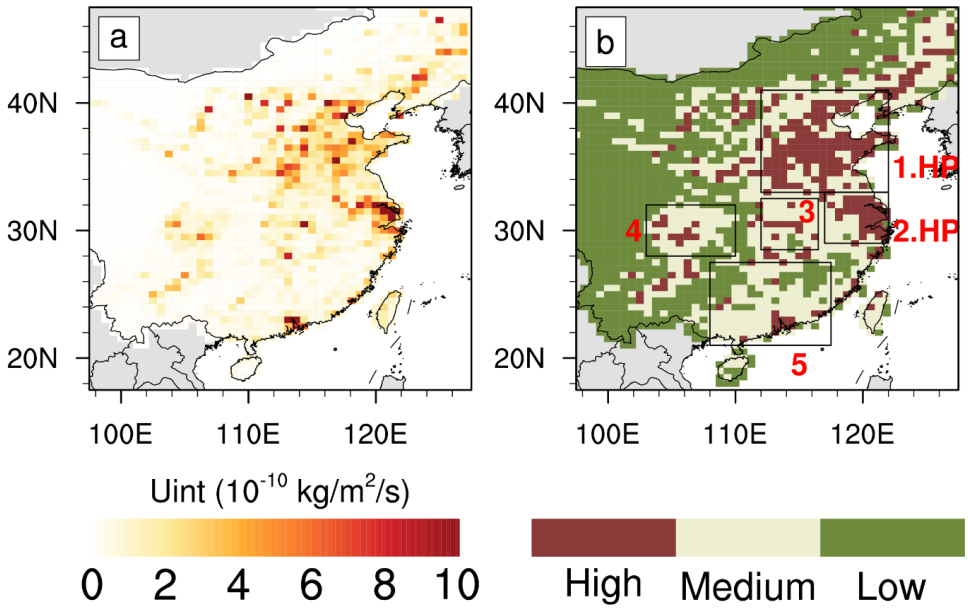

Fig. 1. Anthropogenic NO_x emissions over E. China in 2015; (b) Region definitions for the North China Plain (#1), Yangtze River Delta (#2), Central China (#3), Sichuan Basin (#4) and Southern China (#5). The different colors (red, gray and green) represent grids with high (highest 15%), medium (15-50%) and low (lowest 50%) anthropogenic NO_x emissions. Regions #1 and #2 are defined as highly polluted (HP) regions by excluding grids with low and medium anthropogenic NO_x emissions.

https://doi.org/10.5194/gmd-2023-35
Preprint. Discussion started: 4 April 2023
© Author(s) 2023. CC BY 4.0 License.

Geoscientific Model Development Discussions
Open Access
EGU

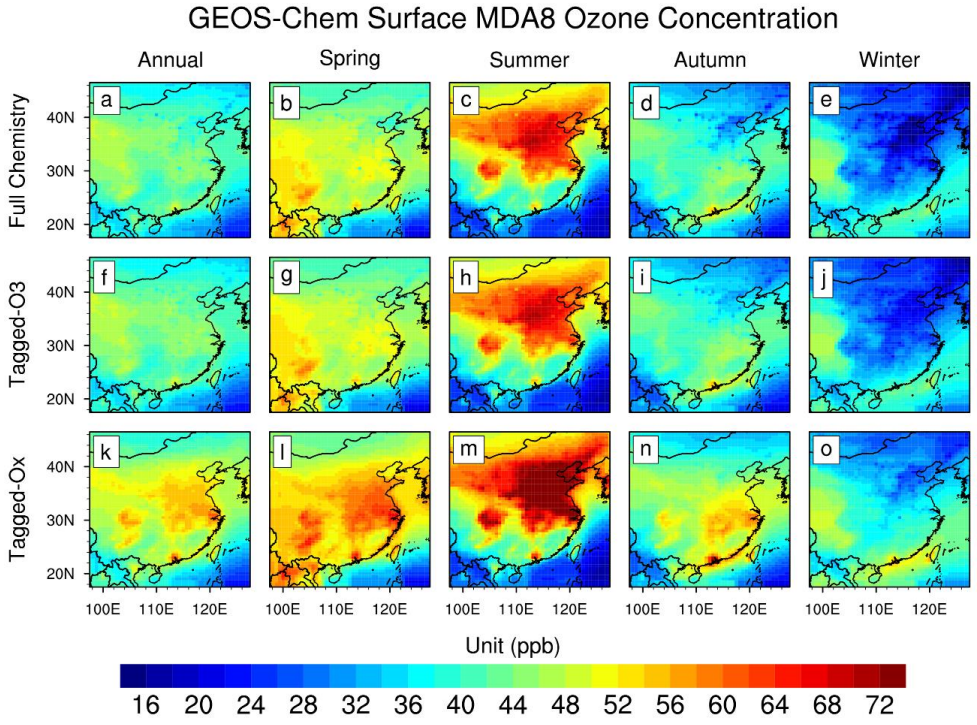

Fig. 2. Surface MDA8 O_3 in 2015-2020 (annual and seasonal averages) simulated by GEOS-Chem model with (A-E) full chemistry mode; (F-J) tagged-O_3 mode; and (K-O) tagged-O_x mode. The 8-hour range of surface O_x is selected according to the time range of MDA8 O_3.

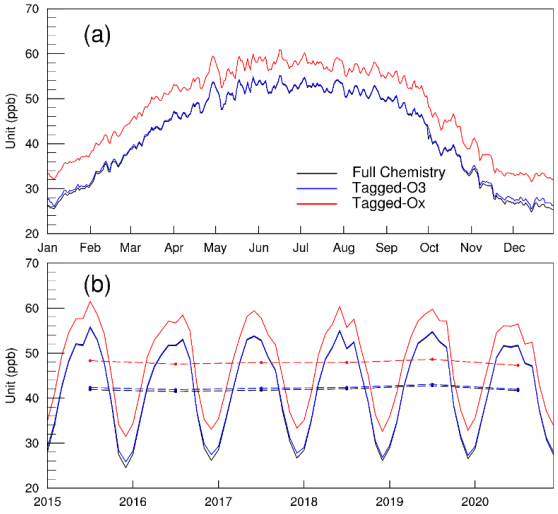

Fig. 3. (A) Daily averages of surface MDA8 O_3 over E. China in 2015-2020 from GEOS-Chem full chemistry (black), tagged-O_3 (blue) and tagged-O_x (red) simulations; (B) Monthly averages of MDA8 O_3. The dashed lines in panel B are annual averages.

https://doi.org/10.5194/gmd-2023-35
Preprint. Discussion started: 4 April 2023
© Author(s) 2023. CC BY 4.0 License.

Geoscientific Model Development
Discussions
Open Access
EGU

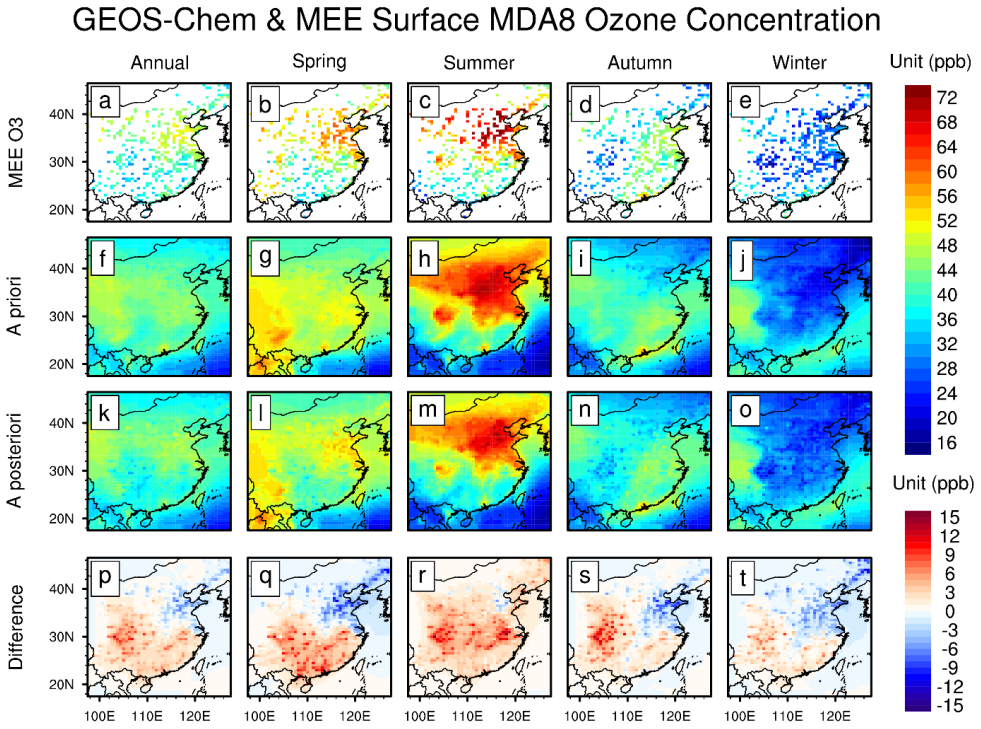

Fig. 4. Surface MDA8 O_3 in 2015-2020 (annual and seasonal averages) from (A-E) MEE stations; (F-J) GEOS-Chem a priori simulation; (K-O) GEOS-Chem a posteriori simulation by assimilating MEE O_3 observations. (P-T) bias in the a priori simulations calculated by a priori minus a posteriori O_3 concentrations.

https://doi.org/10.5194/gmd-2023-35
Preprint. Discussion started: 4 April 2023
© Author(s) 2023. CC BY 4.0 License.

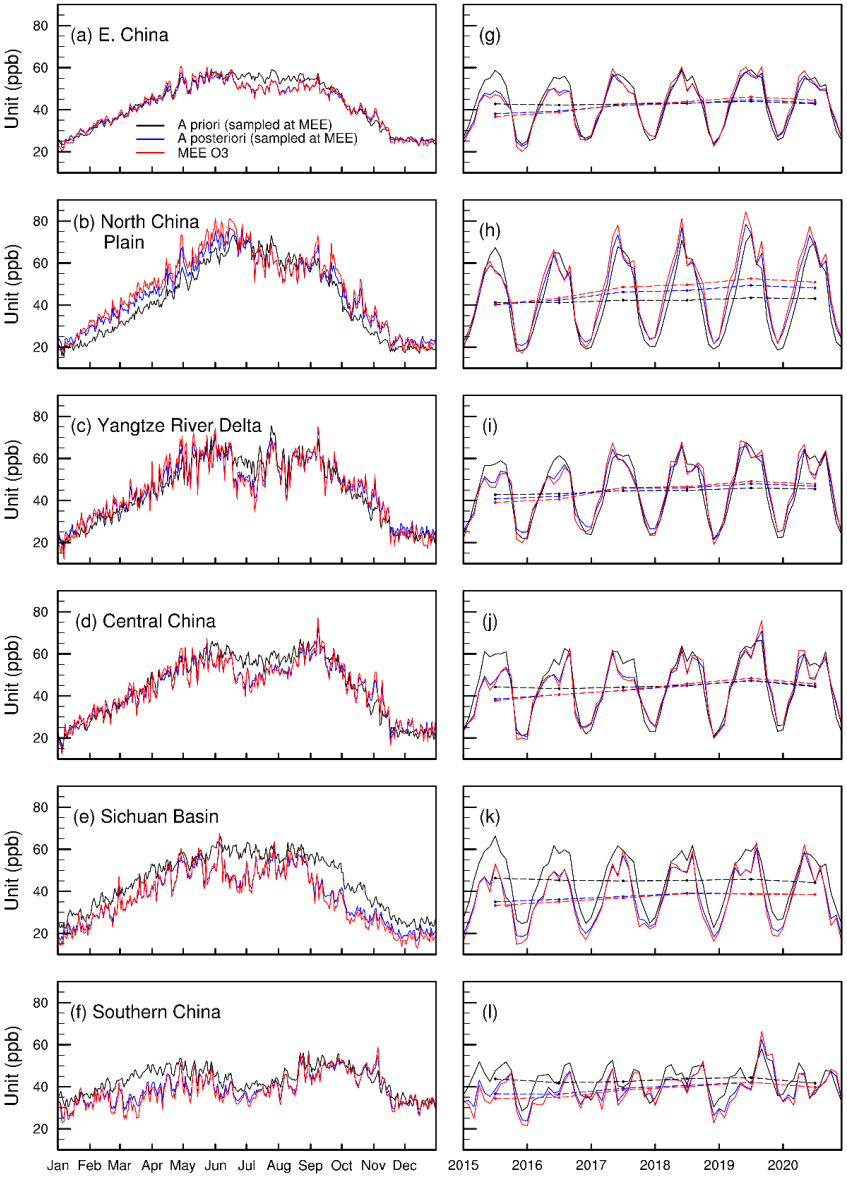

Fig. 5. (A-F) Daily averages of surface MDA8 O_3 in 2015-2020 from MEE stations (red) and GEOS-Chem a priori (black) and a posteriori (blue) simulations by assimilating MEE O_3 observations. (G-L) Monthly averages of MDA8 O_3. The dashed lines in panels G-L are annual averages.

https://doi.org/10.5194/gmd-2023-35
Preprint. Discussion started: 4 April 2023
© Author(s) 2023. CC BY 4.0 License.

Geoscientific Model Development
Discussions
Open Access
EGU

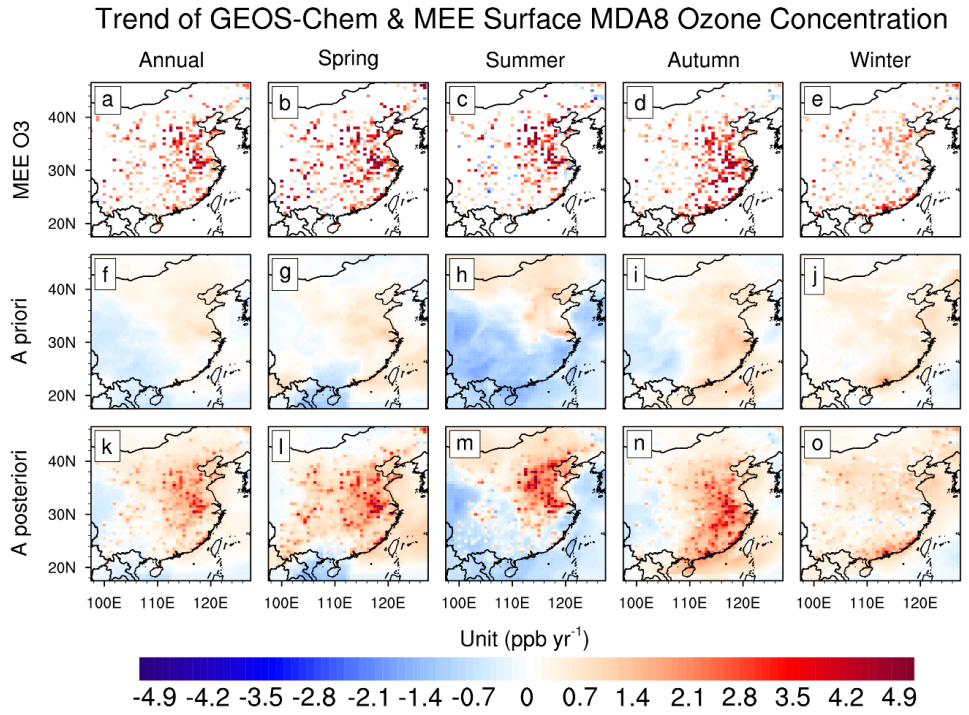

Fig. 6. Trends of surface MDA8 O_3 in 2015-2020 (annual and seasonal averages) from (A-E) MEE stations; (F-J) GEOS-Chem a priori simulation; (K-O) GEOS-Chem a posteriori simulation by assimilating MEE O_3 observations.

https://doi.org/10.5194/gmd-2023-35
Preprint. Discussion started: 4 April 2023
© Author(s) 2023. CC BY 4.0 License.

Geoscientific Model Development
Discussions
Open Access
EGU

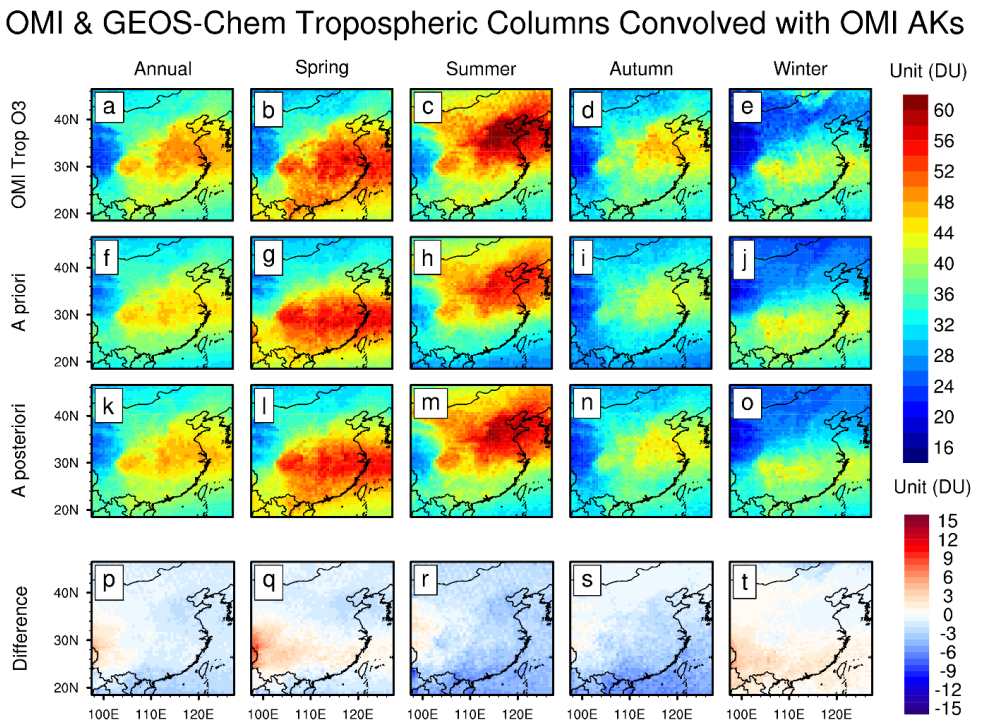

Fig. 7. Tropospheric O_3 columns in 2015-2020 (annual and seasonal averages) from (A-E) OMI observations; (F-J) GEOS-Chem a priori simulation; (K-O) GEOS-Chem a posteriori simulation by assimilating OMI O_3 observations. (P-T) bias in the a priori simulations calculated by a priori minus a posteriori tropospheric O_3 columns. The output O_3 profiles are convolved with OMI averaging kernels.

https://doi.org/10.5194/gmd-2023-35
Preprint. Discussion started: 4 April 2023
© Author(s) 2023. CC BY 4.0 License.

Geoscientific Model Development
Discussions
Open Access
EGU

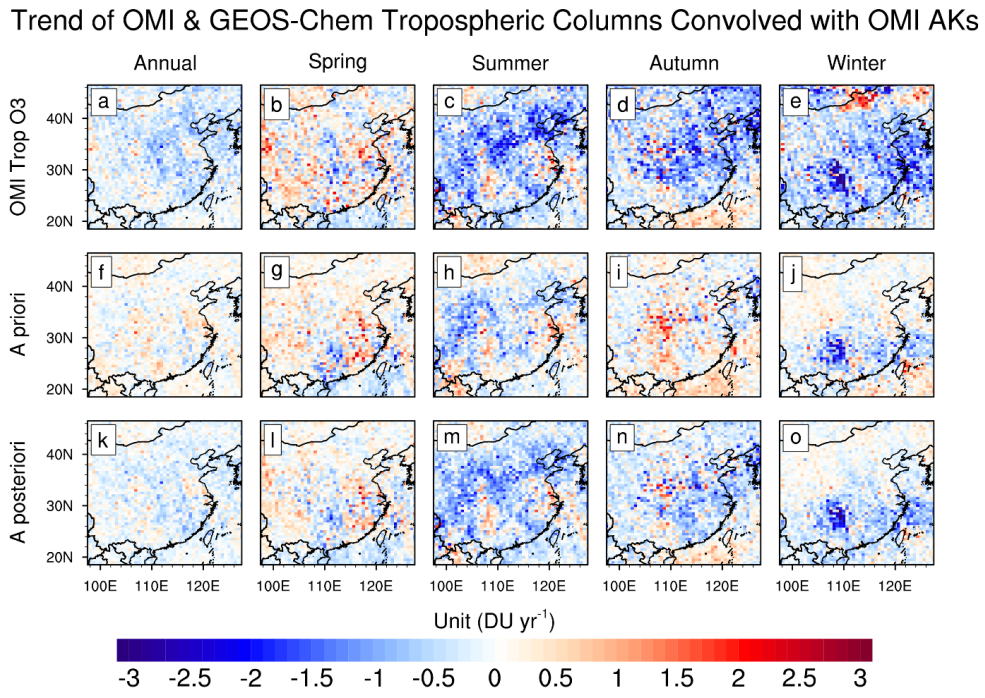

Fig. 8. Trends of tropospheric O_3 columns in 2015-2020 (annual and seasonal averages) from (A-E) OMI observations; (F-J) GEOS-Chem a priori simulation; (K-O) GEOS-Chem a posteriori simulation by assimilating OMI O_3 observations. The output O_3 profiles are convolved with OMI averaging kernels.

https://doi.org/10.5194/gmd-2023-35
Preprint. Discussion started: 4 April 2023
© Author(s) 2023. CC BY 4.0 License.

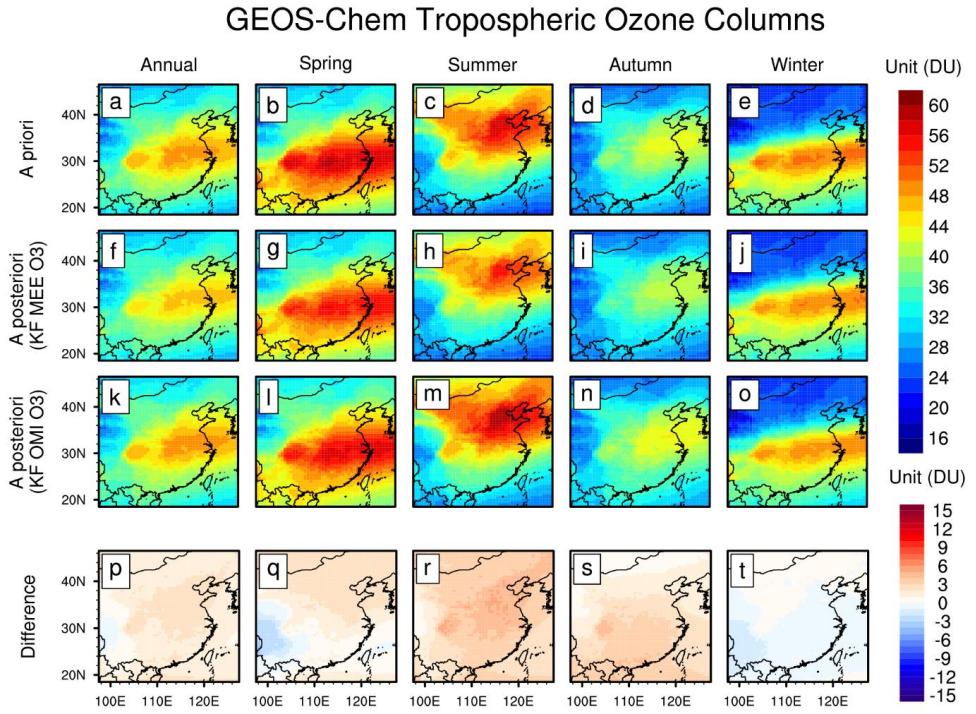

Fig. 9. Tropospheric O_3 columns in 2015-2020 (annual and seasonal averages) from (A-E) GEOS-Chem a priori simulation; (F-J) assimilations of MEE surface O_3 observations; (K-O) assimilations of OMI O_3 observations. (P-T) difference in tropospheric O_3 columns calculated by OMI-based assimilations minus MEE-based assimilations.

https://doi.org/10.5194/gmd-2023-35
Preprint. Discussion started: 4 April 2023
© Author(s) 2023. CC BY 4.0 License.

Geoscientific Model Development
Discussions
Open Access
EGU

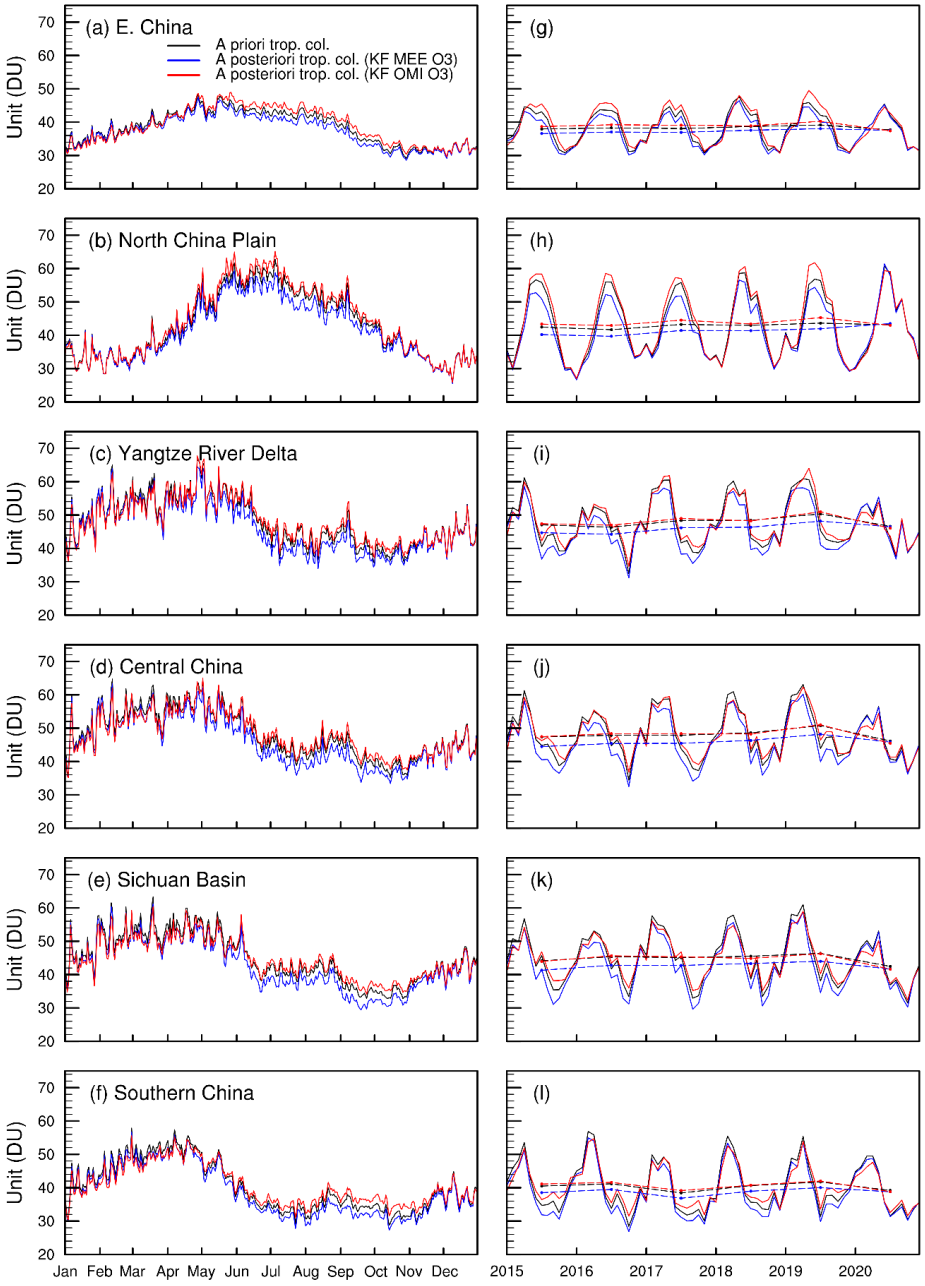

Fig. 10. (A-F) Daily averages of tropospheric O_3 columns in 2015-2020 from GEOS-Chem a priori simulation (black) and a posteriori simulations by assimilating MEE (blue) and OMI (red) O_3 observations. (G-L) Monthly averages of tropospheric O_3 columns. The dashed lines in panels G-L are annual averages.

https://doi.org/10.5194/gmd-2023-35
Preprint. Discussion started: 4 April 2023
© Author(s) 2023. CC BY 4.0 License.

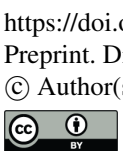

Geoscientific Model Development
Discussions
Open Access
EGU

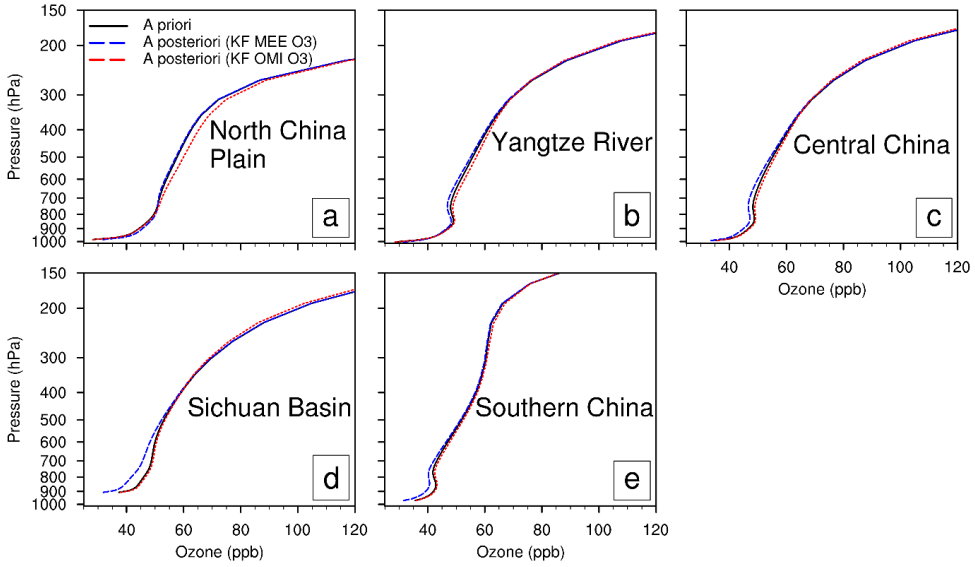

Fig. 11. Averages of O_3 vertical profiles in 2015-2020 from GEOS-Chem a priori (black) and a posteriori simulations by assimilating MEE (blue) and OMI (red) O_3 observations.

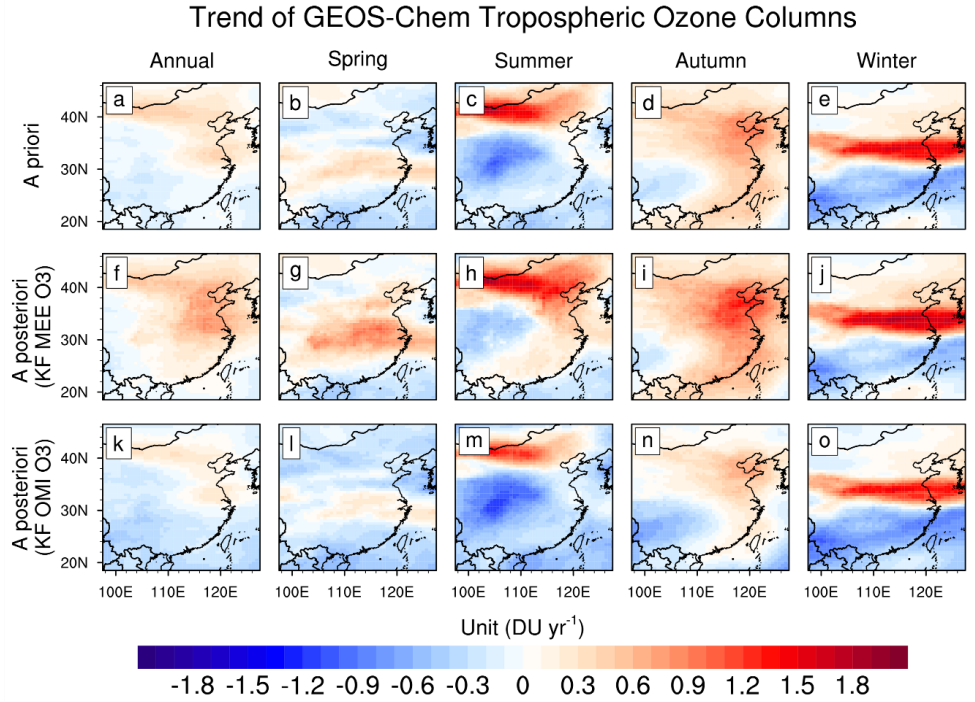

Fig. 12. Trends of tropospheric O_3 columns in 2015-2020 (annual and seasonal averages) from (A-E) GEOS-Chem a priori simulation; (F-J) assimilations of MEE surface O_3 observations; (K-O) assimilations of OMI O_3 observations.